Korean J. Chem. Eng., 38(12), 2423-2435 (2021)
DOI: 10.1007/s11814-021-0902-5

pISSN: 0256-1115
eISSN: 1975-7220

Three-dimensional numerical investigation on the effect of interconnect design on the performance of internal reforming planar solid oxide fuel cell

Hanieh Hesami, Mehdi Borji†, and Javad Rezapour

Department of Mechanical Engineering, Lahijan Branch, Islamic Azad University, Lahijan, Iran
(*Received 8 April 2021 • Revised 3 July 2021 • Accepted 12 July 2021*)

Abstract−Nowadays SOFCs have received great attention due to its advantages such as; high efficiency, low emission and fuel flexibility. But its high operating temperature entails thermal stresses and gas sealing problems which intrigues researchers to reduce the working temperature via thermal management, improved fluid flow, and proper interconnect and channel design. In this study, a three-dimensional model of a co - flow internal reforming planar anode - supported solid oxide fuel cell has been developed. The simulation results are discussed to investigate the performance of different kinds of SOFC flow passages with rectangular, trapezoidal and triangular channels. Also in this study, the effect of inlet fuel and air velocity on the cell performance of the different interconnect ducts is investigated. The results showed that the effect of channel geometry at high voltages is small while, at low voltages channel geometry has an important effect on cell performance. By increasing inlet fuel velocity and decreasing inlet air velocity for all channel geometries, the current and power density and temperature difference increase. Also it was found that, the cells with rectangular channels have better performance than the cells with trapezoidal and triangular channels.

Keywords: Solid Oxide Fuel Cell (SOFC), Anode Supported SOFC, Internal Reforming, Interconnect Design

INTRODUCTION

By definition Solid Oxide Fuel Cell (SOFC) is a highly efficient direct energy conversion device that produces electric power and heat directly from fuel chemical energy through the chemical and electrochemical reactions of fuels and oxidants. Recently, the demand for a solid oxide fuel cell (SOFC) as a power source has increased with the growing concerns about limited resources of conventional fossil fuels and generated harmful chemicals and greenhouse gas emissions [1]. Flexibility in fuel utilization as a result of high operating temperature and possibility of internal reforming of fuel is an advantage of SOFCs over other kinds of fuel cells. To achieve a required voltage and current density in fuel cells a stack must be manufactured by use of various repeated single cells in series or parallel arrangement. High efficiency, low emission, size and fuel flexibility, and low vibration and noise compare with conventional power plants are the main advantages of SOFCs. Improving the structural design of the cell as well as developing new electrode material are two essential ways to increase the SOFC power density [2].

In recent years, different types of fuel cells have been studied. Planer type solid oxide fuel cell is preferred over tubular type due to higher power density and lower electrical resistance. In particular, the anode-supported solid oxide fuel cell with a very thin electrolyte layer greatly reduces ohmic losses. A solid oxide fuel cell consists of two porous layers of cathode and anode with a thin layer of electrolyte between them [3]. In most of the SOFC literature, much research has been done on different aspects of solid oxide fuel cells. Haynes and Wepfer [4] investigated a tubular SOFC and showed that thickening of the electrode plays an important role in the better thermal and electrical performance of SOFC. Borji et al. [5] published a one-dimensional model of a planar anode supported SOFC feed by pre-reformed methane and then the mathematical model is used in a GA optimization procedure to find the best combination of SOFC outputs with respect to some operating parameters. In other studies, performed by Borji et al. [6,7], the integration of SOFC with biomass gasification process and micro gas turbine combined heat and power (CHP) systems have been numerically investigated by an in-house developed program code and optimized. Petersen et al. [8] simulated a solid oxide fuel cell with co current as stable and zero dimensional. In this model, the internal reactions of fuel cell including hydrogen oxidation, methane steam reforming and water - gas shift reactions have been investigated. Aguiar et al. [9,10] developed a model for co- and counter-flow planar cells on the basis of the 1-D mass and heat transfer in fuel and air streams in channels, the 1-D heat transfer in the PEN structure and interconnect, and the 1-D mass transfer of fuel and air species inside the porous electrodes. Their results showed that the temperatures of the PEN structure and interconnect are very close. Thus, the anode, electrolyte, cathode, and interconnect may be considered as a lumped homogenous structure in the heat transfer analysis.

The researches have shown that studies focusing on the effect of gas channel geometries on the SOFCs electric performance are rare in open literature whereas many studies have been carried out on the design of bipolar plates in proton exchange membrane fuel cells (PEM) [11-16]. Lin et al. [17] performed one of the first studies to investigate the effects of ribs on the concentration losses of planar-type fuel cell operations. In this study, it is shown when the rib width

†To whom correspondence should be addressed.
E-mail: mborji@liau.ac.ir

is small, the gas concentration is uniform and electrochemical efficiency is better. Magar and Manglik [18] studied the effect of the depth of the rectangular interconnectors and the thickness of the anode layer on the heat transfer processes of the gas. They concluded that the thermal-hydrodynamic performance of the anode supported SOFC is strongly influenced by the cross - sectional aspect ratio (γ) of the rectangular flow channels and the thickness of the anode layer (λ). Higher convection coefficient, thereby better cooling effect acquirable for shallow channels. Increasing the thickness of the anode layer decreases both thermal and hydrodynamic resistance, resulting in decreasing cell temperature along with the more uniform hydrogen and water mass distribution. Anderson et al. [19] considered rectangular channels for optimization of gas receiving and flow collection. The conservation equations of momentum, gas-phase species, heat, electron and ion transport coupled with complete electrochemical model were solved. In this study the effect of the cathode support layer was determined due to the reduction of the oxygen phase-gas resistance and electron inside the cathode. The result of this study showed that the wider and thinner gas channels reduce the density of the cell current only slightly, but the volumetric cell current significantly increases. Deepra Bhattacharya et al. [20] evaluated the efficiency of different bipolar plate design of 3D planar anode-supported SOFCs. The efficiency of the serpentine and straight geometry of the fuel and air channels of SOFC was compared. They concluded that from the uniformity of ion current density and higher electric efficiency and power point of view, the serpentine flow channels is better than the straight ones, of course these advantages will be accompanying with a big blemish of larger pressure drop. The numerical analysis of an anode supported solid oxide fuel cell with different flow channel design (rectangular, trapezoidal and triangular) was carried out by Manglik and Magar [3]. They revealed that higher heat transfer coefficient and lower friction loss can be seen in fuel flow channel. Also, the forced-convection characteristics (fRe, Nu) are less than the classic ducts. A rectangular channel provides a better cooling effect due to the uniformity of temperature distribution in a SOFC. Also, the fuel and oxide flows in the rectangular channel have higher heat transfer coefficients and lower friction factors (fRe) compared to the triangular and trapezoidal cross - section. Khazaee and Rava [21] investigated the effect of different flow channel geometries on the electric performance of a SOFC. It has been shown that correct distribution of the reactants on the TPB region is significantly affected by the flow channel. Their investigations showed that the efficiency of the anodic and cathodic channels with rectangular geometry is higher compared to the triangle and trapezoidal geometry. The amount of hydrogen consumed is also reduced by increasing the velocity of air and fuel for all geometries. In addition, the results showed that the molar fraction of the hydrogen decreases with increasing the length and the amount of hydrogen molar fraction for the trapezoidal channel is higher than the rectangular and triangular ducts. Kong et al. [2] proposed X-type interconnector and compared it with the conventional interconnector. They concluded that X-type interconnector design can improve the transportation of gaseous specious in SOFC and reduce the current path and thereby enhance the electric performance of the SOFC.

Among the research on geometry of solid oxide fuel cell channels, only the research of Raj Manglik and Magar, as well as Khazaee and Rava, investigated different geometries of the flow channel and they compared the efficiency and heat transfer of different channels. It should be mentioned that in both studies, hydrogen is used as fuel in the anodic channel.

Better electric performance along whit easy fabrication of the planar type SOFC compare to tubular design are the main motives of current study. So in current simulation study, the focus is on the mathematical modeling of direct internal reforming anode-supported planar SOFC behavior and performance. Since the fuel supply is a reformate mixture of natural gas, two main reactions namely, water-gas shift reaction (WGSR) and methane steam reforming reaction (MSRR) must be taken into account.

MSRR:

$$CH_4+H_2O\leftrightarrow CO+3\,H_2 \quad (1)$$

WGSR:

$$CO+H_2O\leftrightarrow CO_2+H_2 \quad (2)$$

The aim of this paper is to develop a detailed mathematical model for the numerical simulation of a methane-fed anode-supported SOFC and investigate the effect of different cross-sectional area of interconnect ducts on flow field of the fuel and oxidant in steady state. In this study, the three-dimensional finite element model is used to optimize the flow channel geometries and sensitive analysis is conducted. Temperature distribution, electrical performance, fuel consumption and mole fraction of the species are the most important investigated parameters.

MODELING

The three dimensional model for an anode-supported SOFC is used to analyze the electrochemical reaction coupled with conservation of gaseous specious mass, momentum, energy and charge. The governing equations are solved by the commercial software COMSOL Multiphysics (version 5.6). Fig. 1 shows a three dimensional SOFC single cell schematically.

The computational domain includes interconnects, fuel and air flow channels, electrodes active and support layer, and electrolyte dividing the total cell into the nine zone. The cell geometry details are listed in Table 1.

1. Assumption

The following assumptions are made in the analysis:

1. The steady state performance of SOFC is modelled.
2. The equal inlet temperature of fuel and air is assumed.
3. Radiation heat transfer is not considered.
4. The temperature dependence of thermal conductivity and heat capacity of gas specious are taken into account.
5. The gas flow within channel and electrode is laminar due to the low velocity.
6. Air and fuel are assumed as perfect gases; therefore, mixture physical properties are obtained from the ideal gas mixture law.
7. To reduce the calculation time, local thermal equilibrium between gas and solid phases within the porous electrodes is considered.
8. Co-flow configuration is modelled in all channel designs.

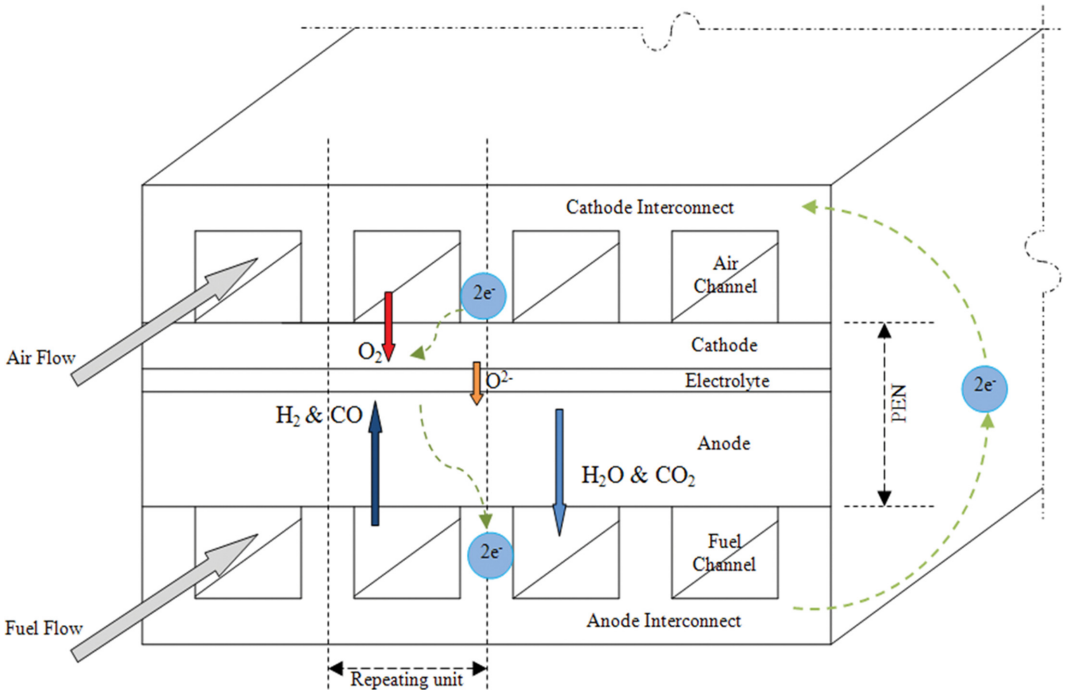

Fig. 1. Schematics of an anode-supported planar-type SOFC.

Table 1. Dimensions of solid oxide fuel cell

Cell geometry parameters	Units	Value
Channel length	mm	100
Fuel/Air channel width	mm	2
Fuel/Air channel height	mm	1
Rib width	mm	0.5+0.5
Interconnect thickness	μm	150+150
Electrolyte thickness	μm	10
Cathode active layer thickness	μm	20
Cathode support layer thickness	μm	50
Anode active layer thickness	μm	15
Anode support layer thickness	μm	400

9. Only the electrochemical reaction of the hydrogen is taken to be account.

10. 30% pre-reformed natural gas consists of 26.26% H_2, 49.34% H_2O, 17.1% CH_4, 2.94% CO, and 4.36% CO_2.

11. Air consists of 79.2% N_2 and 20.8% O_2.

2. Governing Equation

2-1. Charge Conservation Equation

The oxygen as oxidant in cathode and hydrogen as fuel in the anode participate in the electrochemical reaction as the source of electricity [22];

$$\text{At anode: } H_2 + O^{2-} \rightarrow H_2O + 2e^- \tag{3}$$

$$\text{At cathode: } \frac{1}{2}O_2 + 2e^- \rightarrow O^{2-} \tag{4}$$

The fuel and air is supplied in the anode and cathode channel respectively. Reactants are transported to the TPBs, where electrochemical reactions take place. The transfer of ions and electrons respectively are defined by following equations [22-24];

$$i_l = -\sigma_{eff,\,l}\nabla\phi_l \tag{5}$$

$$i_s = -\sigma_{eff,\,s}\nabla\phi_s \tag{6}$$

Where i is the current density, σ_{eff} the effective electron/ion conductivity and ϕ the electron/ion potential. The subscribes l and s mean ion and electron respectively. The electronic conductivities of anode (σ_{Ni}) and cathode (σ_{LSM}) and the ionic conductivity of electrolyte (σ_{YSZ}) can be defined as [22,25,26].

$$\sigma_{Ni} = \frac{9.5\times10^7}{T}\exp\left(\frac{-1150}{T}\right) \tag{7}$$

$$\sigma_{LSM} = \frac{4.2\times10^7}{T}\exp\left(\frac{-1200}{T}\right) \tag{8}$$

$$\sigma_{YSZ} = 3.34\times10^4\exp\left(\frac{-10300}{T}\right) \tag{9}$$

Effective ionic and electronic conductivity of the electrodes can be determined by use of tortuosity factor and volume fractions by [21-23,27];

$$\sigma_{eff,\,a,\,s} = \sigma_{Ni}\cdot\frac{V_{Ni,\,a}}{\tau_{Ni,\,a}} \tag{10}$$

$$\sigma_{eff,\,a,\,l} = \sigma_{YSZ}\cdot\frac{V_{YSZ,\,a}}{\tau_{YSZ,\,a}} \tag{11}$$

$$\sigma_{eff,\,c,\,s} = \sigma_{LSM}\cdot\frac{V_{LSM,\,c}}{\tau_{LSM,\,c}} \tag{12}$$

$$\sigma_{eff,\,c,\,l}=\sigma_{YSZ}\cdot\frac{V_{YSZ,\,c}}{\tau_{YSZ,\,c}} \tag{13}$$

Using electrochemical model, the rate of electrochemical reaction can be calculated for a given operating cell potential (V_{cell}). Cell potential V_{cell} can be determined as equilibrium potential subtracted by all over-potentials. It is assumed that the cell operating voltage is ϕ potential of cathode current collector, whilst for the anodic side the ϕ parameter is zero [28];

$$V_{cell}=E^{OCV}-\eta_{act}-\eta_{ohm}-\eta_{conc} \tag{14}$$

Here V_{cell} means the operating voltage (0.7 V in this paper), η the respective polarization and (E^{OCV}) is the open-circuit voltage that depends on local gas concentration and temperature. This parameter can be calculated by the Nernst equation for a pure hydrogen-steam mixture [9,29].

$$E^{OCV}=E^{0}-\frac{RT}{2F}Ln\left[\frac{P_{H_2O,\,TPB}}{P_{H_2,\,TPB}\sqrt{P_{O_2,\,TPB}}}\right] \tag{15}$$

Where F is the Faraday constant, T the temperature, R the ideal gas constant, P_j the partial pressure of species and E^0 the temperature dependent reversible voltage as shown in Eq. (16) [22,23,27].

$$E^{0}=1.253-2.4516\times10^{-4}T \tag{16}$$

The activation over-potential is on the basis of energy barriers that must be overcome by reacting specious and can be calculated for both anode and cathode electrodes as follows [21,22];

$$\eta_{act,\,a}=\phi_s-\phi_l \tag{17}$$

$$\eta_{act,\,c}=\phi_s-\phi_l-E^{OCV} \tag{18}$$

The index "a" stands for the anode and "c" for the cathode. The concentration over-potential is associated with the specious concentration variation from bulk concentration to the concentration of the specious at the TPBs and can be represented as follows [9,23];

$$\eta_{conc,\,a}=\frac{RT}{n_{e,\,a}\cdot F}Ln\left[\frac{P_{H_2O,\,TPB}\cdot P_{H_2,\,b}}{P_{H_2,\,TPB}\cdot P_{H_2O,\,b}}\right] \tag{19}$$

$$\eta_{conc,\,c}=\frac{RT}{n_{e,\,c}\cdot F}Ln\left[\frac{P_{O_2,\,b}}{P_{O_2,\,TPB}}\right] \tag{20}$$

Where index b stands for the interface between the gas channel and the electrode and the index TPB for the three phase boundary.

Transport of ions and electrons through the electrolyte and electrodes are governed by their ionic and electronic resistivities respectively. Because of these ohmic resistances, there is a voltage loss namely ohmic polarization that given by [24,30]:

$$\eta_{ohm}=R_{tot}\cdot i \tag{21}$$

R_{tot} is the total internal resistance in the cell. Based on the Butler-Volmer equation, following relations can be used for anodic and cathodic sides of SOFC [25,26];

$$i_{v,\,a}=AV_e i_{o,\,ref}^{H_2}\left(\frac{c_{H_2}}{c_{H_2,\,ref}}\right)^{\gamma H_2}\left\{\exp\left[\alpha\frac{n_eF\eta_{act,\,a}}{RT}\right]-\exp\left[-(1-\alpha)\frac{n_eF\eta_{act,\,a}}{RT}\right]\right\} \tag{22}$$

$$i_{v,\,c}=AV_e i_{o,\,ref}^{O_2}\left(\frac{c_{O_2}}{c_{O_2,\,ref}}\right)^{\gamma O_2}\left\{\exp\left[\alpha\frac{n_eF\eta_{act,\,c}}{RT}\right]-\exp\left[-(1-\alpha)\frac{n_eF\eta_{act,\,c}}{RT}\right]\right\} \tag{23}$$

Where AV_e is the electrochemical active area to volume ratio, $i_{o,\,ref}^{H_2}$ and $i_{o,\,ref}^{O_2}$ are reference exchange current density per active surface area for H_2 oxidation and O_2 reduction, c_{H_2} and $c_{H_2,\,ref}$ are H_2 concentration and its reference value; c_{O_2} and $c_{O_2,\,ref}$ are O_2 concentration and its reference value. Here α is the charge transfer coefficient ($0<\alpha<1$), γH_2 and γO_2 are the reaction order for H_2 oxidation and O_2 reduction respectively.

2-2. Species Conservation

Depending on the mean pore diameter of the porous electrodes and comparison of it with mean free path of gas molecules, up to three mass transfer mechanisms; bulk diffusion of gaseous species, diffusion into the porous medium and viscous flow, can be considered. Considering the porous material property of the SOFC, all above mentioned mechanisms must be taken into account. Thus, the conservation of each gaseous species is defined using following equation [23,29]:

$$\rho\frac{\partial}{\partial t}(\omega_i)+\rho(u\cdot\nabla)\omega_i = \nabla\left[\rho\omega_i\sum D_{eff,\,ij}\cdot\nabla x_j+(x_j-\omega_j)\frac{\nabla P}{P}+D_i^T\cdot\frac{\nabla T}{T}\right]+S_i \tag{24}$$

Where ω_i is the mass fraction, x_j the mole fraction, ρ the density is the effective diffusivity coefficient between specie i and j, T is the temperature, D_i^T the thermal diffusion coefficient and S_i the source term for specie i due to electrochemical reactions within the anode and cathode and internal reforming within the anode.

The multi component bulk molecular diffusion coefficients (D_{ij}), for a gas mixture, can be expressed as [21,29];

$$D_{ij}=\frac{k_dT^{1.75}}{P(\nu_i^{1/3}+\nu_j^{1/3})^2}\left[\frac{1}{M_i}+\frac{1}{M_j}\right]^{1/2} \tag{25}$$

Where k_d and ν are reference diffusivity and diffusion volume respectively [29,31,32].

The Knudsen diffusion coefficient ($D_{k,\,ij}$) can be calculated by Eq. (26) [28];

$$D_{k,\,ij}=\frac{2}{3}\bar{r}\sqrt{\frac{8RT}{\pi M_{ij}}} \tag{26}$$

Where $\bar{r}$ is the average pore radius (in this study, $\bar{r}$ is assumed as 0.34 μm), R the universal gas constant and M_{ij} can be calculated as follows [23,28];

$$M_{ij}=\frac{2}{\frac{1}{M_i}+\frac{1}{M_j}} \tag{27}$$

Where M_i and M_j are the molar mass of specie i and j, respectively.

In the porous medium, the tortuous path of the molecule (τ) as well as the porosity factor (ε) can effect strongly the Knudsen and bulk diffusion coefficients. So, the effective diffusion coefficients can be determined as follows [28,33]:

$$D_{eff,\,ij}=\begin{cases}\dfrac{1-x}{\sum_{j\neq i}\dfrac{x_j}{D_{ij}}}, & \text{in gas channels}\\[2ex] \dfrac{\varepsilon}{\tau}\left(\dfrac{1}{\dfrac{\sum_{j\neq i}\dfrac{x_j}{D_{ij}}}{1-x_i}+\dfrac{1}{D_{k,\,ij}}}\right), & \text{in porous electrodes}\end{cases} \tag{28}$$

2-3. Momentum Conservation

The gas mixture flows through the air and fuel channels and diffuses inside porous electrodes. Fluid velocity and pressure variation in the porous electrodes and channels are governed by Darcy-Brinkman equation. In this equation fluid and porous electrodes are treated as a single continuum domain [20,21,25,29]:

$$\frac{\rho}{\varepsilon}\left[\frac{\partial u}{\partial t}+(u\cdot\nabla)\frac{u}{\varepsilon}\right]=-\nabla P+\nabla\cdot\left[\frac{1}{\varepsilon}\left\{\mu(\nabla u+(\nabla u)^T)-\frac{2}{3}\mu(\nabla\cdot u)I\right\}\right]-\left[\frac{\mu}{\kappa}+\frac{Q_{br}}{\varepsilon^2}\right]\cdot u+F \tag{29}$$

$$Q_{br}=\frac{\partial}{\partial t}(\varepsilon\rho)+\nabla\cdot(\rho u) \tag{30}$$

Where ε is the porosity, **F** is the body force vector, μ the dynamic viscosity, κ the permeability of porous medium (1.76×10^{-11} m^2) [34] and Q_{br} is a mass source or sink.

The Darcy-Brinkman equation is transmuted into the well-known Navier-Stokes equation when (ε=1) and ($\kappa\rightarrow\infty$). Thus in the anode and cathode channels Navier-Stokes equation (Eq. (31)) have been used;

$$\rho\frac{\partial u}{\partial t}+\rho u\cdot\nabla u=-\nabla P+\nabla\left[\mu(\nabla u+(\nabla u)^T)-\frac{2}{3}\mu(\nabla\cdot u)I\right]+F \tag{31}$$

$$\nabla\cdot(\rho u)=0 \tag{32}$$

Assuming ideal gas behavior, the density can be expressed as [21,35].

$$\rho=\frac{P\cdot\sum_j x_j\cdot M_j}{R\cdot T} \tag{33}$$

Where x_j is mole fraction of gas phase species j and M_j stands for the molar mass of species. The dynamic viscosities (μ_j) for each species as well as for the gas mixture depend on the local temperature and are calculated as [36]:

$$\mu_j=\sum_{k=1}^{7}b_k\left(\frac{T}{1{,}000}\right)^k \tag{34}$$

$$\mu=\sum_j x_j\cdot\mu_j \tag{35}$$

2-4. Energy Conservation

Regarding high operating temperature of the SOFC, different heat transfer mechanisms within the SOFC and its boundaries must be taken into account [29]. First of all, as considered by many authors, local thermal equilibrium between solid and fluid inside the porous electrodes is assumed [37].

The governing equation for the temperature field is shown in Eq. (36) [22,27,29]. It is worth noting that, because of zero gas velocity only heat conduction within the electrolyte and interconnector is considered;

$$(\rho C_p)_{eq}\frac{\partial T}{\partial t}+\rho C_p u\cdot\nabla T=\nabla\cdot(k_{eq}\nabla T)+Q \tag{36}$$

Where $(\rho C_p)_{eq}$ is the equivalent volumetric heat capacity at constant pressure, (T) is the temperature, C_p the specific heat at constant pressure of the gas mixture, k_{eq} is the equivalent thermal conductivity and Q is the heat source (heat consumption/generation) term.

The specific heat for each gaseous species j and for the gas mixture are defined as [36].

$$C_{p,\,j}=\sum_{K=1}^{7}a_k\left(\frac{T}{1{,}000}\right)^k \tag{37}$$

$$C_p=\sum_j x_j C_{p,\,j} \tag{38}$$

The equivalent thermal conductivity coefficient in the porous electrodes (k_{eq}) consists of a solid conductive coefficient (k_s) and a mixture gas conductive coefficient (k_g) can be calculated as follows [27, 37,38]:

$$k_{eq}=\varepsilon k_g+(1-\varepsilon)k_s \tag{39}$$

Where ε is the porosity. The thermal conductivity coefficient for each gas species j as well as for the gas mixture is defined as [36].

$$k_j=0.01\sum_{K=1}^{7}C_K\left(\frac{T}{1{,}000}\right)^K \tag{40}$$

$$k_g=\sum_i x_j k_j \tag{41}$$

The heat sinks or sources because of internal reforming reactions, the ohmic, activation, and concentration losses, and the entropy change in electrochemical reaction are calculated as [19,22,27]:

$$Q=|i|\cdot\left(\frac{T\cdot|\Delta S_r|}{n_e\cdot F}+|\eta_{act}|+\eta_{conc}\right)+\sum\frac{i^2}{\sigma}+r_{MSR}\Delta H_{MSR}+r_{WGSR}\Delta H_{WGSR} \tag{42}$$

Where ΔS_r is the entropy change for reactions in Eq. (3) and (4), i is the current density, σ is the ion/electron conductivity and n_e the number of electrons transferred per reaction. r_{MSR}, r_{WGSR}, ΔH_{MSR} and ΔH_{WGSR} are the reaction rate and enthalpy change for MSRR and WGSR respectively which are expressed as follows [22,33,39,40]:

$$r_{MSR}=k_{MSR}\cdot\left(P_{H_2O}\cdot P_{CH_4}-\frac{(P_{H_2})^2\cdot P_{CO}}{K_{eq,\,MSR}}\right) \tag{43}$$

$$k_{MSR}=2{,}395\cdot\exp\left(-\frac{231{,}266}{RT}\right) \tag{44}$$

$$K_{eq,\,MSR}=1.0267\times10^{10}\exp(-0.2513Z^4+0.3665Z^3+0.5810Z^2-27.134Z+3.277) \tag{45}$$

$$r_{WGSR}=k_{WGSR}\cdot\left(P_{H_2O}\cdot P_{CO}-\frac{P_{H_2}\cdot P_{CO_2}}{K_{eq,\,WGSR}}\right) \tag{46}$$

$$k_{WGSR}=0.0171\exp\left(\frac{-103{,}191}{RT}\right) \tag{47}$$

Table 2. Parameters used in this paper

Parameters	Units	Values
Electrochemistry parameters		
Ion conducting volume fraction [19]		0.42
Electron conducting volume fraction [19]		0.28
Porosity [19]		0.3
Ion conducting tortuosity factor [19]		10
Electron conducting tortuosity factor [19]		10
Gas-phase tortuosity factor [19]		3
Reference exchange current density for H_2 oxidation [26]	A/m^2	1,320
Reference exchange current density for O_2 reduction [26]	A/m^2	400
Reference H_2 concentration [25]	mol/m^3	10.78
Reference O_2 concentration [25]	mol/m^3	2.38
Reaction order for H_2 oxidation [25]		0.5
Reaction order for O_2 reduction [25]		0.5
Diffusion parameters		
Diffusion volume H_2 [31]	cm^3/mol	6.12
Diffusion volume O_2 [31]	cm^3/mol	16.3
Diffusion volume N_2 [31]	cm^3/mol	18.5
Diffusion volume CO_2 [31]	cm^3/mol	26.9
Diffusion volume CO [31]	cm^3/mol	18
Diffusion volume CH_4 [32]	cm^3/mol	25.14
Diffusion volume H_2O [31]	cm^3/mol	13.1
Reference diffusivity [21]	m^2/s	3.16e-8

$$K_{eq,\,WGSR}=\exp(-0.2935Z^3+0.6351Z^2+4.1788Z+0.3169) \quad (48)$$

$$Z=\frac{1{,}000}{T}-1 \quad (49)$$

$$\Delta H_{MSR}=-(206{,}205.5+19.5175T) \quad (50)$$

$$\Delta H_{WGSR}=45{,}063-10.28T \quad (51)$$

The consumption of fuel in SOFCs is defined as the ratio of the amount of fuel that electrochemically consumes to the amount of inlet fuel stream.

$$C_{fuel}=\frac{x_{fuel,\,0}-x_{fuel,\,end}}{x_{fuel,\,0}} \quad (52)$$

$$x_{fuel}=x_{H_2}+x_{CO}+4x_{CH_4} \quad (53)$$

Here x_j is the mole fraction of species j.

3. Input Parameters and Boundary Conditions

The cell geometry, operating conditions and cell other reference parameters are listed in Tables 1, 2, and 3. Fuel channel feed by a 30% pre-reformed natural gas which produces in turn a syngas consisting of H_2, CH_4, CO_2, CO, and H_2O. On the other side, the air consisting of oxygen and nitrogen flows through the air channel. Convective heat flux and pressure outlet are assumed as the channel outlet boundary condition, whilst at the inlet, specified temperature (1,023 K) and velocity inlet are defined. The inlet fuel and air velocity is 0.3 m/s and 3 m/s respectively. The ionic current density is zero at the interfaces between electrodes support and activation layers and at the interfaces between electrodes activation layer and electrolyte the electronic current density is zero.

Table 3. Solid material parameters of solid oxide fuel cell

Solid material parameters	Units	Values
Anode thermal conductivity [27]	w/mK	11
Cathode thermal conductivity [27]	w/mK	6
Electrolyte thermal conductivity [27]	w/mK	2.7
Interconnect thermal conductivity [27]	w/mK	20
Anode specific heat [27]	J/kgK	450
Cathode specific heat [27]	J/kgK	430
Electrolyte specific heat [27]	J/kgK	470
Interconnect specific heat [27]	J/kgK	550
Anode density [23]	Kg/m^3	3,310
Cathode density [23]	Kg/m^3	3,030
Electrolyte density [23]	Kg/m^3	5,160
Interconnect density [23]	Kg/m^3	3,030

The electrode potential at the anode and cathode current collector is zero and cell voltage (operating voltage) varies from 0.55 to 0.8 V.

RESULT AND DISCUSSION

The commercial software COMSOL multiphysics based on finite element method has been used to solve above mentioned system of conservation equations with given data in Tables 1, 2, and 3 and boundary conditions as discussed.

With the purpose of validation, current model predictions have been compared with the experimental results reported by NIMTE

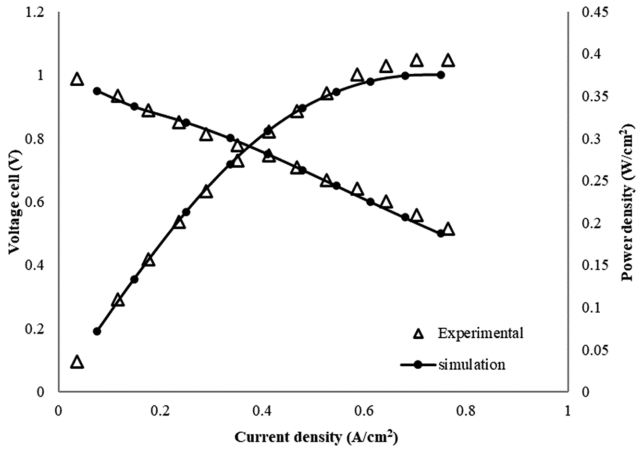

Fig. 2. Comparison of predicted V-I and P-I characteristics between model-predicted and experimental data.

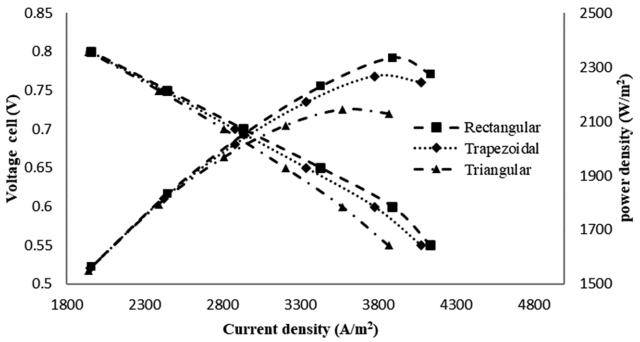

Fig. 4. The influence of channel shapes on the cell performance.

[41]. For the experiments fuel and air flow rates are 800 sccm and 2,000 sccm respectively. The overpotentials and power density at different current densities obtained using present model are compared to the experimental results as illustrated in Fig. 2. As it can be seen, results match well with those of experimental results of NIMTE [41].

In this section, the performance of three channel shapes (rectangular- trapezoidal- triangular) have been studied for different cell voltages [0.8, 0.75, 0.7, 0.65, 0.6, 0.55 V] and over a range of fuel and air velocity keeping all other operating conditions identical. The fuel and air velocity has been increased gradually from 0.2 to 0.7 m/s and 3 to 8 m/s respectively. The channel geometries are shown in Fig. 3.

1. Effect of Channel Shapes on the Performance of Cell

To study the effect of different channel shapes on SOFCs performance, the simulation of each case was carried out for six different cell voltages [0.8, 0.75, 0.7, 0.65, 0.6, 0.55 V]. Fig. 4 shows the polarization and the power density curves for the three different geometrical shapes (rectangular- trapezoidal- triangular) of the flow channel. This figure shows that at higher voltages the polarization curves are almost coincident with each other, i.e. the effect of channel geometry at high voltages is small, while at lower voltages the effect of different geometry of fuel and air channels is important. On the other hand, the cells with rectangular channels show better performance than the trapezoidal and triangular channels due to more uniform distribution and better penetration of reactant gases and increasing the rate of electrochemical reaction. Also, the cells with triangular channel have the weakest performance so that the current density at the operating voltage of 0.55 V for the cell with rectangular channel is more than 6% higher compared to triangular channel whereas for the cell voltage 0.8 V, this increase is less than 1%. Furthermore, the cells with rectangular channels have the highest power density over the trapezoidal and triangular channels.

2. Effect of Channel Shapes on the Fuel Consumption and Temperature Difference

Fig. 5 shows the effect of different channel shapes on cell fuel consumption and temperature difference. An increased operational potential means less voltage available for the various losses, consequently the current density decreases according to Eqs. (22) and (23). As observed, the fuel consumption and the temperature difference decreases with increasing the cell voltage for each of the three different geometry of the channel. Also, as shown in Fig. 5, the cells with rectangular channels have higher fuel consumption and temperature difference because of better performance and higher power and current density than other flow channel geometries. Moreover, at higher cell voltages, fuel consumption and the tem-

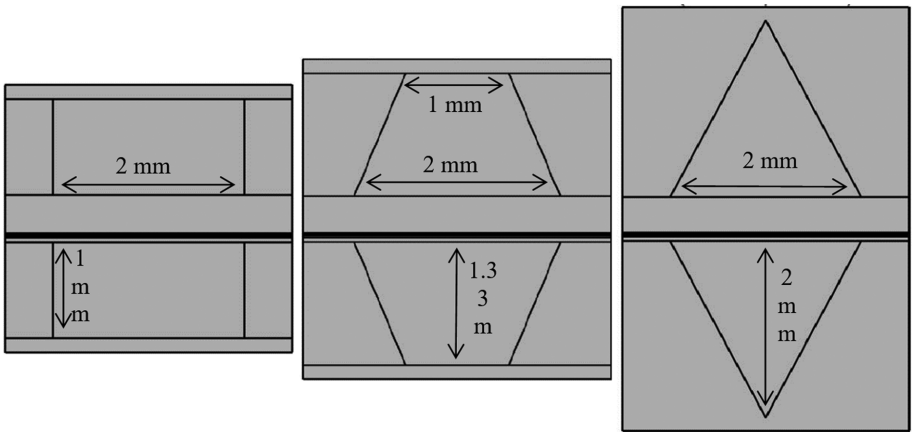

Fig. 3. 2D Schematic of different flow channel cross section shape.

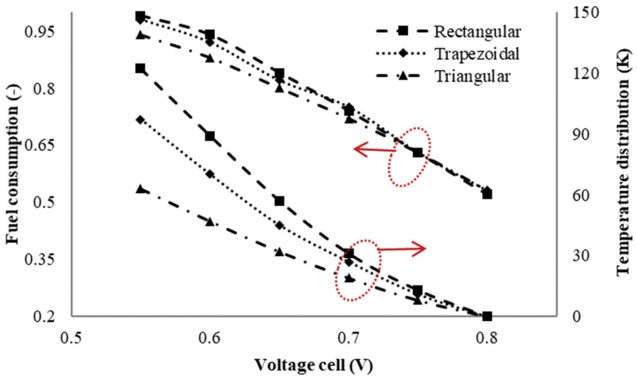

Fig. 5. The influence of channel shapes on the fuel consumption and temperature distribution.

perature difference for all three channel shapes differ slightly. By reducing operating voltage, differences between these curves become more apparent. For example, for cell voltage of 0.55 volts, when the channels geometry changes from triangular and trapezoidal to rectangular, the fuel cell temperature difference increases 94% and 26% respectively.

3. Effect of Channel Shapes on the Anode Species Distribution

Fig. 6 shows the species distribution of the cell feed by a 30% pre-reformed natural gas at the fuel channel-anode interface for three shapes of the interconnect duct (triangular, trapezoidal, or rectangular) at working voltage of 0.7 V. In general, for three shapes of the interconnect duct, the hydrogen mole fraction in the main direction of the flow reduces from its initial value of 0.2626 due to the electrochemical reactions near the anode/electrolyte interface but increases due to methane steam reforming (MSR) and water gas shift reaction (WGSR) within the anode. Water is consumed in reforming reaction (MSR and WGSR) and generated in the electrochemical reactions, hence as it is shown in Fig. 6, the water mole fraction increases. Methane is consumed in MSR thus, reduces in the main direction of flow. Note that due to intermediate operat-

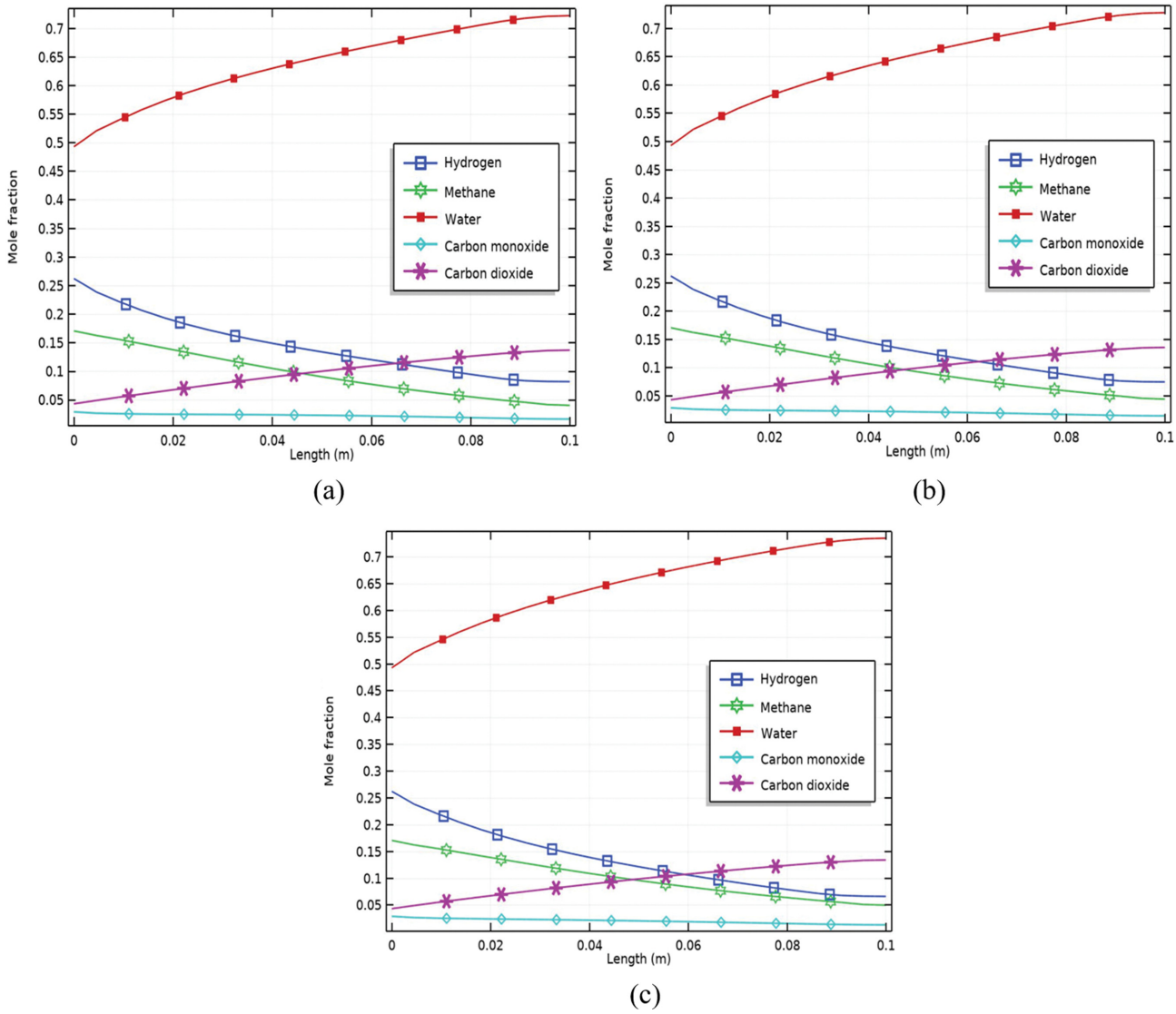

Fig. 6. Mole fraction distributions along the flow direction for (a) rectangular channel (b) trapezoidal channel (c) triangular channel.

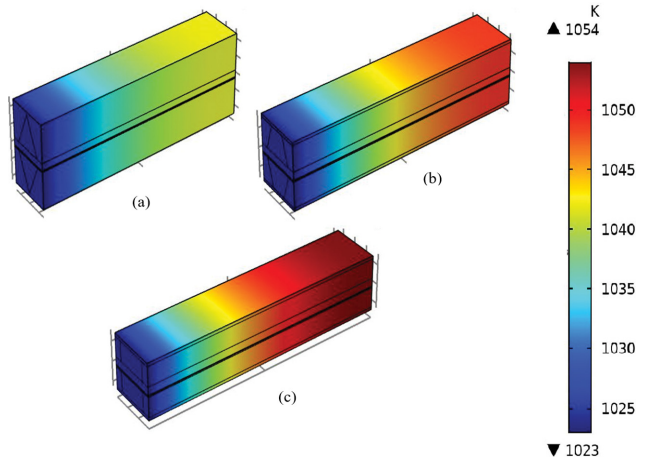

Fig. 7. Temperature distribution (K) along the main flow direction for (a) triangular channel (b) trapezoidal channel (c) rectangular channel.

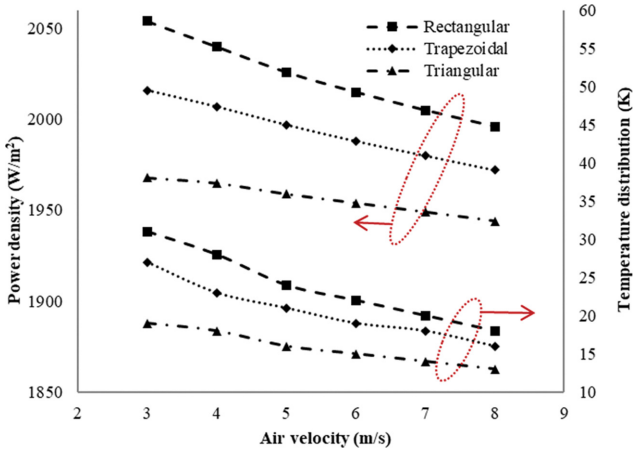

Fig. 8. The influence of inlet air velocity on the temperature distribution and power density of the different interconnect ducts.

ing temperature, all methane doesn't convert to hydrogen and carbon dioxide. Carbon monoxide is consumed in WGSR but generated in MSR. Carbon dioxide is generated in water gas shift reaction and transformed to the fuel channel through the porous anode and then to the outside of the cell. Also, as indicated in the Fig. 6, the molar fraction of the reactants in the anode, for all three rectangular, triangular and trapezoidal channels, do not differ much and the trend of mole fraction in all three channels is almost the same, however there are few changes in the graphs. For example, the hydrogen mole fraction of the triangular channel is more reduced but, the methane mole fraction, which has the highest impact on the fuel consumption, has less reduction than other channels. As a result, at the working voltage of 0.7 V, the fuel cell with triangular channel has the lowest fuel consumption coefficient (0.72).

4. Effect of Channel Shapes on the Distribution of Cell Temperature

Fig. 7 depicts the distribution of temperature of the fuel cell with different channel geometries (rectangular, triangular and trapezoidal shape) at working voltage of 0.7 V along the cell. As observed, for all three channel shapes, the temperature increases in the flow main direction. The temperature is increases in the main direction of flow due to electrochemical reaction, activation, concentration and ohmic losses, and the WGSR and decreases due to highly endothermic methane reforming reaction, however as shown in this figure, the cell with rectangular channel has higher temperature difference because of higher current density than the trapezoidal and triangular channels so that the temperature difference in the cell with rectangular channel is 15% and 63% higher than those of the cells with trapezoidal and triangular channels respectively.

5. Effect of Air Velocity on Performance of Cell

The influence of inlet air velocity on the temperature difference and power density of the different interconnect ducts (rectangular, triangular and trapezoidal) is shown in Fig. 8. Increased air flow rate means increased cooling effect and causes decreasing the temperature of the cell, electrochemical and MSR reaction rate and thus, as seen in Fig. 8, for all three geometries, this reduction leads to current and power density reduction. On the other hand, the amount of oxygen penetration in the cathode decreases due to the increase of the inlet air velocity and therefore a large amounts of gases exhausted from the cell without any electrochemical reaction. This leads to decrease in current and power density and decrease of temperature difference. Also, it is found from Fig. 8 that the cell with rectangular channel has the highest power density and maximum temperature difference compared to triangular and trapezoidal channels. In addition, it is concluded that the slope of the power density and the temperature difference curve of the fuel cell with rectangular channel is greater than those of the trapezoidal and triangular channels so that with a 167% increase in the inlet air velocity, the power density of the cells with rectangular, trapezoidal and triangular channels will decrease 2.8%, 2.2% and 1.2% respectively.

6. Effect of Fuel Velocity on the Performance of Cell

Fig. 9 shows the effect of inlet fuel velocity on the fuel consumption and power density of the different interconnect ducts. As it can be seen, for all three channel geometries, as the fuel inlet speed increases, the power density increases. By increasing the fuel flow

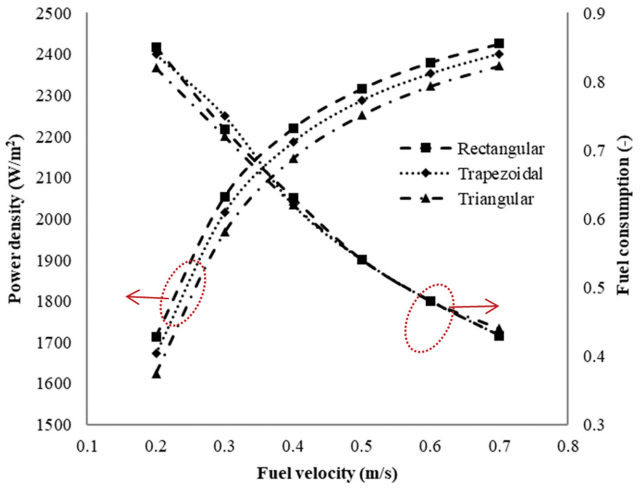

Fig. 9. The influence of inlet fuel velocity on the fuel consumption and power density of the different interconnect ducts.

rate, the rate of electrochemical reaction increases which entails increasing the cell current and power density. Of course, as shown in Fig. 9, the cells with rectangular channels have the highest power density compared to other considered shapes. But increasing the inlet fuel speed has an adverse effect on fuel consumption coefficient. At high inlet fuel velocities, a large fraction of the fuel flow leaves the gas channel without performing an electrochemical reaction due to the low chance of diffusion through the electrodes. It is important to note that the channel geometry has no effect on the fuel consumption coefficient especially in high fuel velocities.

The effect of inlet fuel velocity on the current density and temperature difference for all three fuel and air duct geometries (rectangular, triangular and trapezoidal shapes) are shown in Fig. 10. As mentioned earlier, the electrochemical reaction rate increases as a result of increased fuel velocity and thus the temperature difference and current density increase. Thus, by increasing the inlet fuel flow velocity, for each of the three channel geometry, both current density and temperature difference have an increasing trend. As it can be concluded from Fig. 10, the cells with rectangular channels have more current density and temperature difference than other channels in all fuel velocities. It is noted that the slope of all curves is higher for lower velocities. As the velocity increases, the slope decreases so that for the inlet fuel velocities greater than 0.5 m/s, the temperature difference for each of the three channel geometry remains constant as the fuel velocity increases.

Figs. 11, 12 and 13 depict the change of electrode current density with inlet fuel velocity for three considered duct geometries at the cathode-electrolyte interface. There are some important points in these figures. Firstly, the current density is much higher close to the entrance of the channel for all three duct geometries. This indicated that the electrochemical reaction mainly occur close to the channel inlet. The rate of electrochemical reaction also decreases with decreasing hydrogen concentration along the channel. The

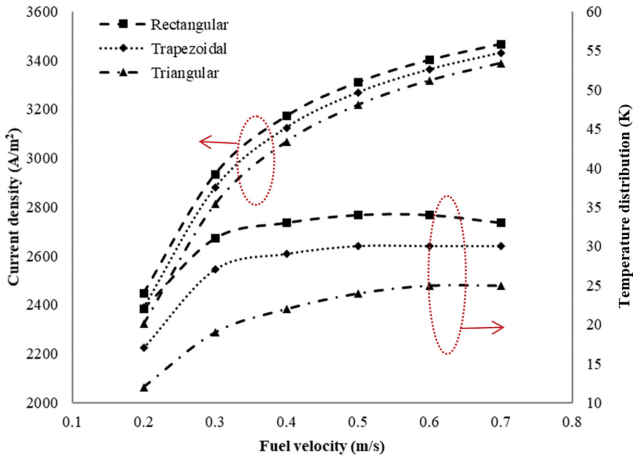

Fig. 10. The influence of inlet fuel velocity on the temperature distribution and current density of the different interconnect ducts.

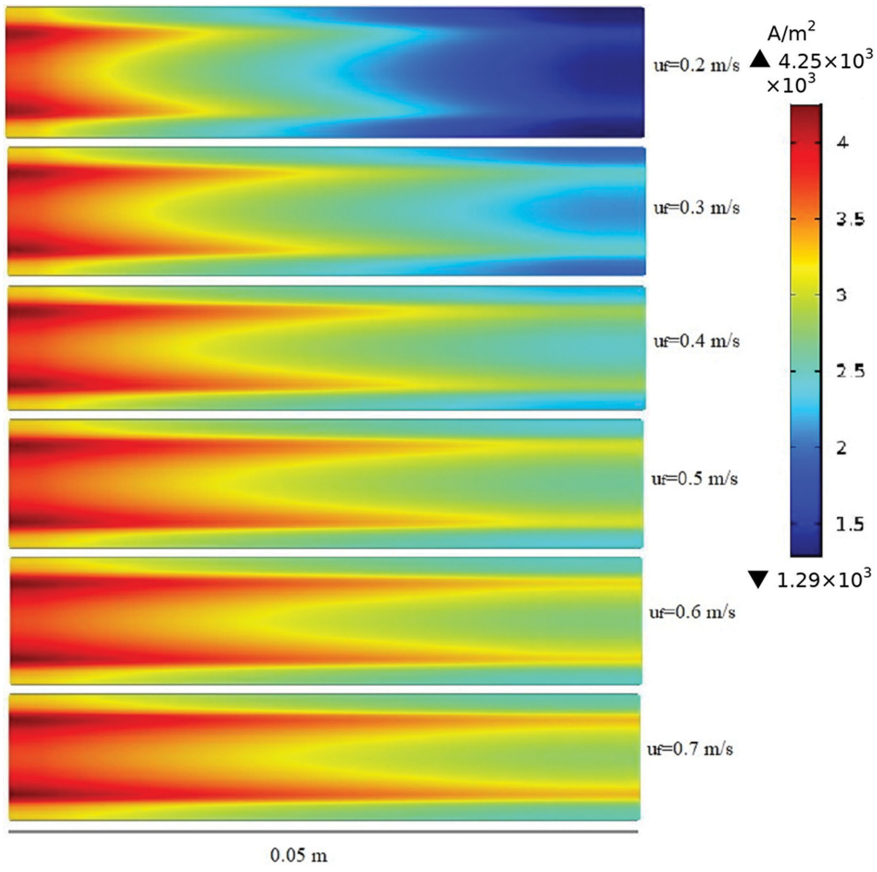

Fig. 11. Variation of electrode current density (A/m^2) distribution for various inlet fuel velocities for rectangular channel.

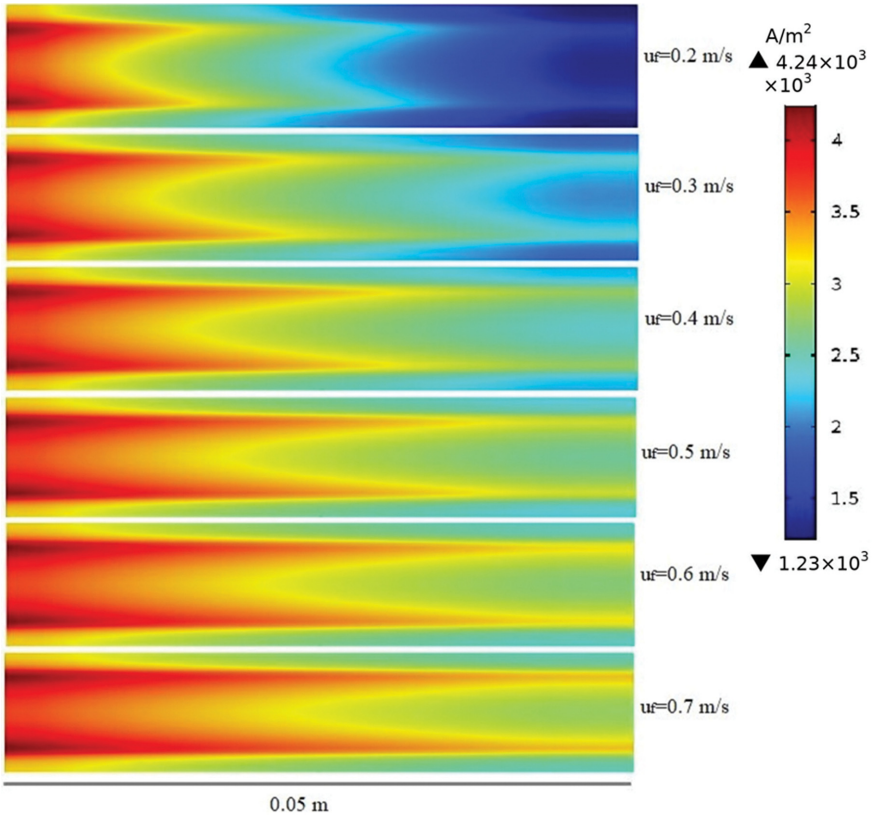

Fig. 12. Variation of electrode current density (A/m^2) distribution for various inlet fuel velocities for trapezoidal channel.

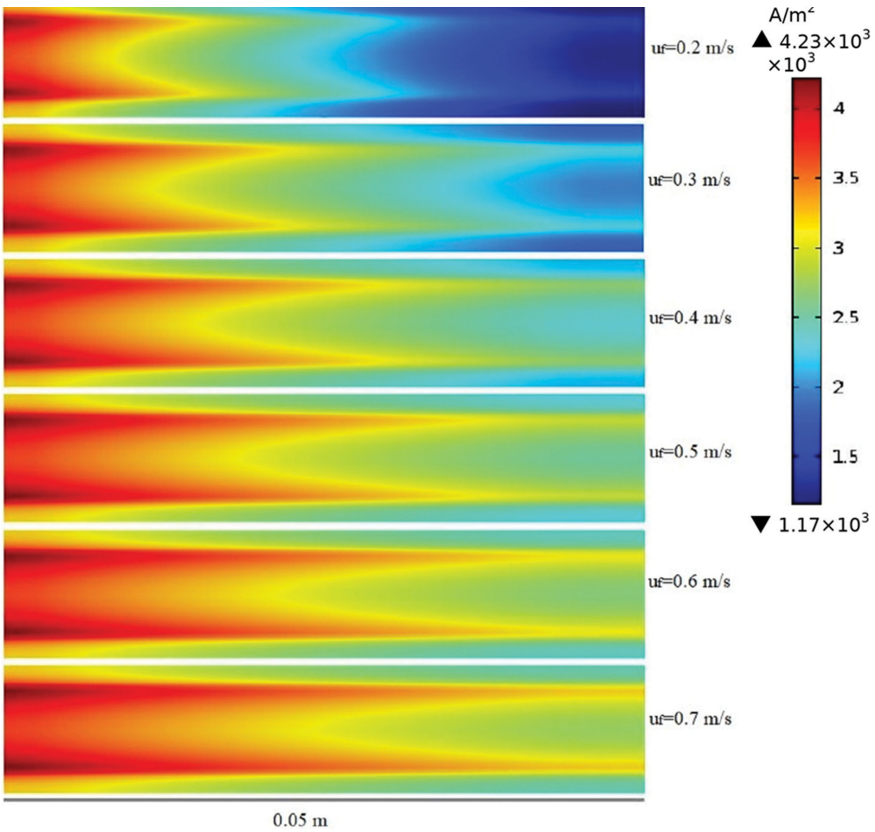

Fig. 13. Variation of electrode current density (A/m^2) distribution for various inlet fuel velocities for triangular channel.

current density is reduced in the main flow direction with oxygen and hydrogen consumption and water production. Secondly, as shown in these figures due to low oxygen concentration, the current density is low for area under the rib. Also, the highest current density is observed in the cathode/interconnect ribs corner due to the high concentration of oxygen and short electron transfer distance. On the other hand, as indicated in these figures, the electrode current density increases as the inlet fuel flow rate increases for all the considered cases so that with an increase of 250 percent of the inlet fuel velocity, the average electrode current density at the cathode/electrolyte interface for the cell with rectangular, trapezoidal and triangular channel is increased by 34%, 35% and 37% respectively.

CONCLUSION

A three-dimensional SOFC model has been formulated considering the main conservation equations of; energy, specious mass, momentum and electron and ion. Imposing proper boundary conditions, the system of conservation equations has then been solved by use of commercial software COMSOL Multiphysics based on finite element method. This simulation includes interconnects, air and fuel flow channels, electrodes active and support layers, and electrolyte. The model has been validated against available experimental data. The simulation results are discussed to investigate the performance of solid oxide fuel cells with three different duct geometries (rectangular, triangular and trapezoidal). The most important results obtained from such finite element based modeling for an anode-supported internal reforming SOFC can be concluded as follows;

- The effect of channel geometry at high voltages is small while at low voltages channel geometry has an important effect on cell performance so that the current density at the operating voltage of 0.55 V for the fuel cell with rectangular channel is more than 6% higher compared to triangular channel. Also, at the same voltage, by changing the shape of the fuel and air duct from triangular and trapezoidal channel to the rectangular channel, the cell temperature difference is increased 94% and 26%, respectively.
- For all three channel shapes, the temperature raises in the flow main direction of the cell. This increase in fuel cell with rectangular duct is higher than the cells with trapezoidal and triangular channels at cell voltage 0.7 V, 15% and 63% respectively.
- By increasing the inlet air velocity for all three geometries, the current and power density and cell temperature difference decreases so that with a 167% increase in the inlet air velocity, the power density of the cells with rectangular, trapezoidal and triangular channels will decrease 2.8%, 2.2% and 1.2% respectively. In addition, the cells with rectangular channels have higher temperature difference and current density.
- By increasing the inlet fuel velocity for all three geometries, fuel consumption coefficient decreases but the cell temperature difference, power and current density increases so that with an increase of 250% of the inlet fuel velocity, the average electrode current density at the cathode/electrolyte interface for the cell with rectangular, trapezoidal and triangular channel is increased by 34%, 35% and 37% respectively. Also, the channel geometry has no effect on the fuel consumption coefficient especially in high fuel velocities.
- With regard to the discussions that have been made, the fuel cell with a rectangular channel relative to other channels has the maximum current and power density, fuel consumption coefficient and the temperature difference however, increasing the temperature difference increases the thermal stresses and reduces cell life time. Since in most cases the temperature difference in the fuel cell with a rectangular channel is not so high, so the cell has better performance than the cells with trapezoidal and triangular channels.

NOMENCLATURE

AV_e : active area to volume ratio [$m^2 \cdot m^{-3}$]
c_{H_2} : hydrogen concentration [$mol \cdot m^{-3}$]
$c_{H_2, ref}$: reference hydrogen concentration [$mol \cdot m^{-3}$]
c_{O_2} : oxygen concentration [$mol \cdot m^{-3}$]
$c_{O_2, ref}$: reference oxygen concentration [$mol \cdot m^{-3}$]
C : consumption of fuel
C_p : specific heat at constant pressure [$J \cdot kg^{-1} \cdot K^{-1}$]
D_{ij} : binary diffusion coefficient [$m^2 \cdot s^{-1}$]
$D_{k, ij}$: Knudsen diffusion coefficien [$m^2 \cdot s^{-1}$]
$D_{eff, ij}$: effective diffusion coefficient [$m^2 \cdot s^{-1}$]
E^0 : ideal voltage before partial pressure consideration [V]
E^{OCV} : ideal voltage after partial pressure consideration [V]
F : volume force vector [$N \cdot m^{-3}$]
F : Faraday's constant [96485.3 $C \cdot mol^{-1}$]
ΔH : enthalpy change of reaction [$J \cdot mol^{-1}$]
i : current density [$A \cdot m^{-2}$]
$i_{o, ref}^{H_2}$: reference exchange current density for H_2 oxidation [$A \cdot m^{-2}$]
$i_{o, ref}^{O_2}$: reference exchange current density for O_2 reduction [$A \cdot m^{-2}$]
k_d : reference diffusivity [$m^2 \cdot s^{-1}$]
k : thermal conductivity [$W \cdot m^{-1} \cdot K^{-1}$]
M_j : molecular weight of species j [$kg \cdot mol^{-1}$]
n_e : number of electrons transferred per reaction
P : pressure [Pa or bar]
Q : heat source or sink [$W \cdot m^{-3}$]
Q_{br} : mass source or sink [$kg \cdot m^{-3} \cdot s^{-1}$]
$\bar{r}$: pore radius [m]
r : reaction rate [$mol \cdot m^{-3} \cdot s^{-1}$]
R : gas constant [8.314 $J \cdot mol^{-1} \cdot K^{-1}$]
ΔS_r : entropy change due to chemical reaction [$J \cdot mol^{-1} \cdot K^{-1}$]
T : temperature [K]
u : mass averaged velocity [$m \cdot s^{-1}$]
V_{cell} : cell voltage [V]
V : volume fraction
x : molar fraction
x, y, z : Cartesian coordinates

Greek Symbols

α : charge transfer coefficient
γH_2 : reaction order for H_2 oxidation
γO_2 : reaction order for O_2 reduction
ε : porosity
η : over potential [V]
ϕ : potential [V]

κ : permeability [m^2]
μ : dynamic viscosity [pa·s]
ν : molecular diffusion volume [$cm^3 \cdot mol^{-1}$]
ρ : density [$kg \cdot m^{-3}$]
σ : ionic/electronic conductivity [$\Omega^{-1} \cdot m^{-1}$]
τ : tortuosity
ω : mass fraction

Subscripts
0 : initial
a : anode
act : activation
c : cathode
conc : concentration
eff : effective
eq : equivalent
g : gas-phase
i : (gas-phase) molecule i
j : (gas-phase) molecule j
k : Knudsen diffusion
MSR : methane steam reforming reaction
l : electrolyte material
ohm : ohmic
s : solid-phase, electrode material
tot : total
WGSR : water gas shift reaction

DECLARATION OF INTERESTS

We wish to confirm that there are no known conflicts of interest associated with this publication and there has been no significant financial support for this work that could have influenced its outcome.

REFERENCES

1. J. M. Park, D. Y. Kim, J. D. Beak, Y.-J. Yoon, P.-Ch. Su and S. H. Lee, *Energies*, **11**, 473 (2018).
2. W. Kong, Z. Han, S. Lu, X. Gao and X. Wang, *Int. J. Hydrogen Energy*, **45**, 20329 (2020).
3. R. M. Manglik and Y. N. Magar, *J. Thermal Sci. Eng. Appl.*, **7**, 041003 (2015).
4. C. Haynes and W. J. Wepfer, *Int. J. Hydrogen Energy*, **26**, 369 (2001).
5. M. Borji, K. Atashkari, N. Nariman-zadeh and M. Masoumpour, *Proc. Inst. Mech. Eng., Part C*, **229**, 3125 (2015).
6. M. Borji, K. Atashkari, S. Ghorbani and N. Nariman-zadeh, *Proc. Inst. Mech. Eng., Part C*, **231**, 672 (2017).
7. M. Borji, K. Atashkari and N. Nariman-zadeh, *Int. J. Hydrogen Energy*, **40**, 14202 (2015).
8. T. F. Petersen, N. Houbak and B. Elmegaard, *Int. J. Thermodyn.*, **9**, 147 (2006).
9. P. Aguiar, C. S. Adjiman and N. P. Brandon, *J. Power Sources*, **138**, 120 (2004).
10. P. Aguiar, C. S. Adjiman and N. P. Brandon, *J. Power Sources*, **147**, 136 (2005).
11. X. Li and I. Sabir, *Int. J. Hydrogen Energy*, **30**, 359 (2005).
12. H. Heidary and M. J. Kermani, *Int. Commun. Heat Mass Transfer*, **39**, 112 (2012).
13. H. Heidary, A. Abbassi and M. J. Kermani, *Energy Convers. Manag.*, **75**, 748 (2013).
14. H. Heidary and M. J. Kermani, *Int. J. Hydrogen Energy*, **38**, 5485 (2013).
15. H. Liu, P. Li and K. Wang, *Int. J. Hydrogen Energy*, **38**, 9835 (2013).
16. M. Dehsara and M. Kermani, *J. Mech. Sci. Technol.*, **28**, 365 (2014).
17. Z. Lin, J. W. Stevenson and M. A. Khaleel, *J. Power Sources*, **117**, 92 (2003).
18. Y. N. Magar and R. M. Manglik, *J. Fuel Cell Sci. Technol.*, **4**, 185 (2007).
19. M. Andersson, J. Yuan and B. Sundén, *Fuel Cells*, **14**, 177 (2014).
20. D. Bhattacharya, J. Mukhopadhyay, N. Biswas, R. Nath Basu and P. Kumar Das, *Int. J. Heat Mass Transfer*, **123**, 382 (2018).
21 I. Khazaee and A. Rava, *Energy*, **119**, 235 (2017).
22. Sh. Zeng, X. Zhang, J. S. Chen, T. Li and M. Andersson, *Int. J. Heat Mass Transfer*, **125**, 506 (2018).
23. M. Andersson, J. Yuan and B. Sundén, *Int. J. Heat Mass Transfer*, **55**, 773 (2012).
24. K. Takino, Y. Tachikawa, K. Mori, S. M. Lyth, Y. Shiratori, S. Taniguchi and K. Nagasaki, *Int. J. Hydrogen Energy*, **45**, 6912 (2020).
25. J. Shi and X. Xue, *Chem. Eng. J.*, **163**, 119 (2010).
26. M. M. Hussain, X. Li and I. Dincer, *J. Power Sources*, **161**, 1012 (2006).
27. M. Andersson, H. Paradis, J. Yuan and B. Sundén, *Electrochim. Acta*, **109**, 881 (2013).
28. Y. Wang, R. Zhan, Y. Qin, G. Zhang, Q. Du and K. Jiao, *Int. J. Hydrogen Energy*, **43**, 20059 (2018).
29. A. N. Celik, *Int. J. Hydrogen Energy*, **43**, 19730 (2018).
30. T. Choudhary and Sanjay, *Int. J. Hydrogen Energy*, **41**, 10212 (2016).
31. B. E. Poling, J. M. Prausnitz and J. P. O'Connell, *The properties of gases and liquid*, McGraw-Hill companies Inc, New York (2001).
32. A. Dutta, *Multicomponent gas diffusion and adsorption in coals for enhanced methane recovery*, Ms.c. Thesis, Department of energy resources engineering, Standford University (2009).
33. M. Ni, *Energy Convers. Manag.*, **70**, 116 (2013).
34. S. Kakaç, A. Pramuanjaroenkij and X. Y. Zhou, *Int. J. Hydrogen Energy*, **32**, 761 (2007).
35. M. Ebadi Chelmehsara and J. Mahmoudimehr, *Int. J. Hydrogen Energy*, **43**, 15521 (2018).
36. B. Todd and J. B. Young, *J. Power Sources*, **110**, 186 (2002).
37. S. Lee, H. Kim, K. J. Yoon, J.-W. Son, J.-H. Lee, B.-K. Kim, W. Choi and J. Hong, *Int. J. Heat Mass Transfer*, **97**, 77 (2016).
38. A. Pramuanjaroenkij, S. Kakac and X. Zhou, *Int. J. Hydrogen Energy*, **33**, 2547 (2008).
39. B. A. Haberman and J. B. Young, *Int. J. Heat Mass Transfer*, **47**, 3617 (2004).
40. B. Lin, Y. Shi, M. Ni and N. Cai, *Int. J. Hydrogen Energy*, **40**, 3035 (2015).
41. M. Andersson, J. Yuan, B. Sundén, T. Sh. Li and W. G. Wang, Proceedings of ASME Fuel Cell Science, Engineering and Technology Conference Fuel Cell, Washington, DC, USA (2011).